

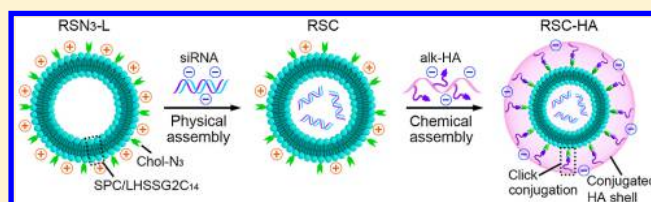
# A Collaborative Assembly Strategy for Tumor-Targeted siRNA Delivery

Qiong Sun, Zisheng Kang, Lingjing Xue, Yunkai Shang, Zhigui Su, Hongbin Sun, Qineng Ping, Ran Mo,\* and Can Zhang\*

State Key Laboratory of Natural Medicines and Jiangsu Key Laboratory of Drug Discovery for Metabolic Diseases, Center of Drug Discovery, China Pharmaceutical University, Nanjing 210009, China

**S** Supporting Information

**ABSTRACT:** A novel “collaborative assembly” approach was reported for the synthesis of an siRNA delivery system via a combination of an electrostatically driven physical assembly and a facile click reaction-mediated chemical assembly, which showed various advantages of more safety, efficiency, and flexibility over the conventional approach that is only based on the physical assembly. This strategy remained a high cationic property of lipid-based complex for high siRNA loading capacity. The direct chemical modification of a model polyanion, hyaluronic acid (HA) on the cationic complex via click chemistry shielded the positive charge of complex without affecting the siRNA binding, which reduced the toxicity and enhanced the blood stability of the complex. In addition, the incorporated polyanion might be prefunctionalized, which endowed the carrier with better biological characteristics such as long circulating or tumor targeting. We demonstrated that the obtained lipid-polymer hybrid nanoparticle (RSC-HA) using collaborative assembly presented greater *in vivo* stability in the blood for efficient tumor targeting than the physically assembled RSC/HA in which HA was physically adsorbed on the complex. After endocytosis into the cells, the protection of RSC-HA on siRNA turned off, while the release of siRNA induced by the intracellular signals for enhanced gene-silencing capacity. This combination of physical and chemical assemblies provides an efficient strategy for the exploitation of safe, stable, and functionalized siRNA delivery systems.



## INTRODUCTION

Small interfering RNA (siRNA) has emerged as a promising therapeutic agent for targeted cancer therapy due to its potent gene-silencing activity.<sup>1,2</sup> Naked siRNA has been proven to be unfavorable for systemic delivery due to its inherent limitations such as labile degradation by blood nucleases and rapid elimination by renal excretion.<sup>3</sup> Up to now, although arduous efforts have been made,<sup>4–7</sup> no commercial siRNA product is on the market for intravenous cancer treatment.<sup>8,9</sup> The development of a safe and efficient siRNA delivery system still remains to be a critical challenge.

Viral and nonviral carriers have been widely reported for siRNA delivery.<sup>10,11</sup> Although the viral vectors show high transfection capability, their applications are enormously limited by serious immunotoxicity and adverse effects.<sup>12,13</sup> Cationic lipids and polymers as the most common nonviral vectors used for siRNA delivery can efficiently assemble with siRNA via electrostatic adsorption to form a condensed complex, which provides enhanced cellular uptake and higher siRNA-mediated gene-silencing effect.<sup>14–18</sup> The development of cationic carrier-based siRNA delivery systems is highly dependent upon the management of the relationship among cationic property, toxicity, siRNA binding efficiency, and stability.<sup>19</sup> Higher cationic carriers result in stronger siRNA binding rates with higher stabilities. However, such complex with high positive surface charge often induces complement

activation and inflammatory response after intravenous administration, thereby yielding severe toxicities *in vivo*.<sup>20,21</sup> Reducing positive charge may alleviate the toxicities, in part, but affects the stability of the complex yet.<sup>22,23</sup> Moreover, not only can negatively charged blood proteins easily bind onto the cationic complex,<sup>24</sup> which interferes with the complex stability in the circulation, but also competitively displace negatively charged siRNA in the complex, which impedes the therapeutic efficacy of siRNA.

To solve this issue, the most practical strategy is PEGylation of the cationic lipids/polymers or noncovalent coating with polyanions to shield the high positive charge of the complex.<sup>25–27</sup> Nevertheless, the steric hindrance of the incorporated PEG chain decreases the siRNA binding with the cationic carrier and also hampers the tumor cell uptake of the carrier.<sup>28,29</sup> Additionally, the PEGylated nanoparticles suffer from the accelerated blood clearance and lose their long-circulating properties after consecutive intravenous injections.<sup>30</sup> For the polyanionic coating as a physical layer-by-layer (LbL) assembly approach, the incorporation of polyanions with higher negative charge inevitably disturbs the electrostatic interaction between cationic constituents and anionic siRNA by competitive binding to the complex, which causes the leakage of

Received: February 9, 2015

Published: April 14, 2015

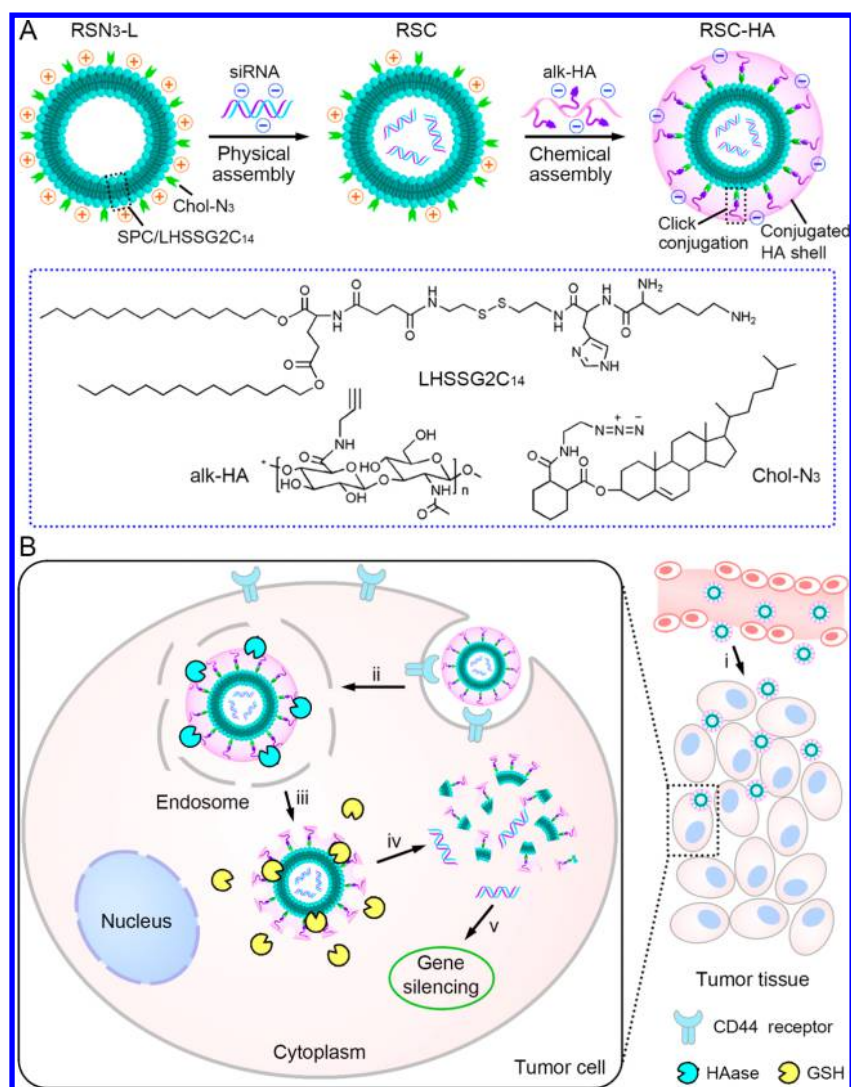


**Figure 1.** (A) Schematic illustration of the “collaborative assembly” strategy for construction of an siRNA delivery system consisting of a lipid-polymer hybrid nanocarrier via a combination of an electrostatically driven physical assembly and a click reaction-mediated chemical assembly. (B) Schematic illustration of tumor-targeted siRNA delivery by RSC-HA. (i) Accumulation of RSC-HA at the tumor site; (ii) endocytosis of RSC-HA into the tumor cells; (iii) HAase-mediated degradation of the HA shell of RSC-HA and endosomal escape into the cytoplasm; (iv) GSH-triggered disassembly of RSC-HA and release of the complexed siRNA in the cytoplasm; and (v) gene silencing induced by the released siRNA.

preloaded siRNA and the reduction in the siRNA loading capacity.<sup>22,23</sup> Furthermore, the exterior polyanions are inclined to be displaced by the negatively charged proteins in the blood, leading to aggregation and elimination by the reticular epithelial system.<sup>31,32</sup> Accordingly, this physical assembly strategy that mainly depends upon the electrostatic force cannot realize an effective siRNA delivery as expected. To address the dilemma in the cationic property-associated toxicities, siRNA binding efficiency, and stability, a new assembly strategy for siRNA packing and delivery is highly desirable.

Herein, we report a novel “collaborative assembly” approach for synthesis of an siRNA delivery system consisting of a lipid-polymer hybrid nanocarrier via a combination of an electrostatic force-based physical assembly and a facile click reaction-mediated chemical assembly, which has a variety of advantages over the above-mentioned physical assembly method: (1) the high cationic property of the lipid is remained without chemical modification such as PEGylation, which renders the high siRNA binding and loading capacity; (2) the direct chemical decoration of polyanion on the cationic vector shows no

influence on the binding between siRNA and the carrier, which can shield the cationic property, reduce the toxicity, and improve the blood stability of the complex; (3) the incorporated polyanion may be prefunctionalized with PEG or ligands, which endues carriers with better biological behaviors such as long circulating or tumor targeting.

The chemical assembly is based on the azide–alkyne cycloaddition click chemistry.<sup>33,34</sup> Cholesterol (Chol) as a commonly used component for liposome preparation and hyaluronic acid (HA) as a model polyanion with good biocompatibility and biodegradability are functionalized with azide and alkyne groups as clickable modules, respectively. The azide-modified cholesterol (Chol-N<sub>3</sub>) with a natural soy phosphatidylcholine (SPC) and a reduction-cleavable cationic lipid (LHSSG2C<sub>14</sub>) is first used to fabricate a dual-functionalized cationic liposome with redox responsiveness and clickability, which is further mixed with siRNA to form a complex (designated as RSC) via the electrostatically driven assembly (Figure 1A). The anionic alkyne-modified HA (alk-HA) is readily coated on RSC, followed by the rapid click

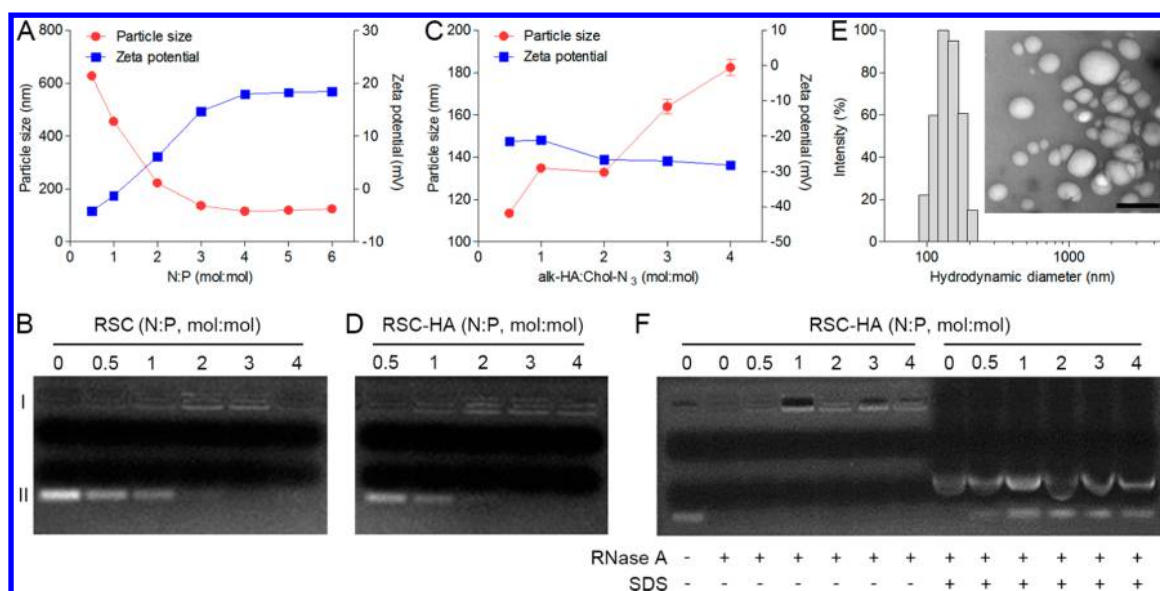


**Figure 2.** (A) Particle size and  $\zeta$  potential of RSC at different N:P ratios. (B) Agarose gel electrophoresis assay of RSC at different N:P ratios: (I) the complexed siRNA band and (II) the free siRNA band. (C) Particle size and  $\zeta$  potential of RSC-HA with siRNA at different ratios of alk-HA:Chol-N<sub>3</sub>. (D) Agarose gel electrophoresis assay of RSC-HA (alk-HA:Chol-N<sub>3</sub> = 2:1, mol:mol) at different N:P ratios. (E) Size distribution histogram of RSC-HA (N:P = 4:1, mol:mol; alk-HA:Chol-N<sub>3</sub> = 2:1, mol:mol) using the DLS measurement. Inset: TEM image of RSC-HA. Scale bar: 200 nm. (F) Agarose gel electrophoresis assay of RSC-HA at different N:P ratios in the absence or presence of RNase A or SDS.

reaction-mediated coupling to achieve a stable HA-conjugated RSC (RSC-HA) without the leakage of siRNA. HA also serves as an active tumor-targeting ligand, which can bind to the cell surface receptors such as CD44 that is overexpressed in many tumors.<sup>35</sup> Moreover, HA can be degraded by hyaluronidase (HAase) in the tumor intracellular compartments to “turn off” the protective function of HA, contributing to the exposure and release of the payloads.<sup>36</sup>

As illustrated in Figure 1B, RSC-HA after intravenous administration is expected to have a good colloidal stability and preferentially accumulate at the tumor site by the combined passive and active targeting effects. After internalization by the tumor cells into the endosomes, the HA shell of RSC is degraded by HAase and sheds from RSC. Meanwhile, the LHSSG2C<sub>14</sub> component promotes endosomal escape of RSC due to the proton sponge effect of the imidazole ring of histidine,<sup>37</sup> which allows migration of RSC into the cytoplasm. The high cytoplasmic concentration of GSH further cleaves the disulfide bond in LHSSG2C<sub>14</sub> via the thiol–disulfide exchange,<sup>38</sup> which leads to the liposomal destabilization along with the RSC disassembly and therefore triggers the release of the encapsulated siRNA in the cytoplasm for gene silencing. This combination of physical and chemical assemblies provides an efficient strategy for the exploitation of safe, stable, and functionalized siRNA delivery systems.

## RESULTS AND DISCUSSION

**Collaborative Assembly of RSC-HA.** The reduction-sensitive cationic lipid, LHSSG2C<sub>14</sub> (Scheme S1 in the Supporting Information), the nonreduction-sensitive cationic lipid, LHG2C<sub>14</sub> (Scheme S2), and two clickable modules, Chol-N<sub>3</sub> (Scheme S3) and alk-HA (Scheme S4) were first synthesized and characterized by <sup>1</sup>H nuclear magnetic resonance spectroscopy. The azide-decorated redox-sensitive cationic liposome (designated as RSN<sub>3</sub>-L) consisting of SPC, LHSSG2C<sub>14</sub> and Chol-N<sub>3</sub> (5:5:3, w:w:w) was prepared using the thin-film hydration method. RSN<sub>3</sub>-L was mixed with siRNA

at the optimal N:P ratio of 4:1 (the molar ratio of nitrogen in RSN<sub>3</sub>-L to phosphate in siRNA) via electrostatic adsorption to form RSC, which had an average particle size of 117 nm and a  $\zeta$  potential of +18 mV (Figure 2A). The encapsulation of siRNA by RSC was confirmed by the electrophoretic mobility shift assay (EMSA) (Figure 2B). No free siRNA was observed on the siRNA band, indicating that the siRNA molecules were completely complexed with RSN<sub>3</sub>-L. Subsequently, RSC was added into the alk-HA solution at a molar ratio of alk-HA:Chol-N<sub>3</sub> of 2:1 to obtain a negatively charged alk-HA-coated RSC, followed by click reaction catalyzed by the *in situ* generation of active copper(I) species from reduction of copper sulfate by sodium ascorbate (Figure 2C). The collaboratively assembled RSC-HA (N:P = 4:1, mol:mol) was finally achieved after removal of the catalysts by centrifugal filtration. No undesirable release and destruction of the encapsulated siRNA were determined after the click reaction-mediated assembly (Figure 2D). The obtained RSC-HA (alk-HA:Chol-N<sub>3</sub> = 2:1, mol:mol) had a hydrodynamic diameter of about 130 nm and a  $\zeta$  potential of –26 mV. The transmission electron microscope (TEM) examination showed a spheroid structure of RSC-HA (Figure 2E). The chemical assembly of HA on the RSC surface was further demonstrated by both the disappearance of the characteristic infrared absorption peak of azide group at 2101 cm<sup>-1</sup> (Figure S1A) and the increased ultraviolet absorbance resulting from generation of triazole group after click reaction (Figure S1B). To evaluate the protection of siRNA by RSC-HA from nuclease degradation, RSC-HA was incubated with ribonuclease A (RNase A), which is commonly present in the blood, for 30 min at 37 °C, followed by the EMSA analysis (Figure 2F). Free siRNA was rapidly digested by RNase A, while RSC-HA showed a high capability of protecting siRNA from the RNase A degradation.

To validate the higher stability of the collaboratively assembled RSC-HA than the physically assembled complex, we took the unmodified HA-coated RSC complex with siRNA (designated as RSC/HA) as a control, which had a resulting

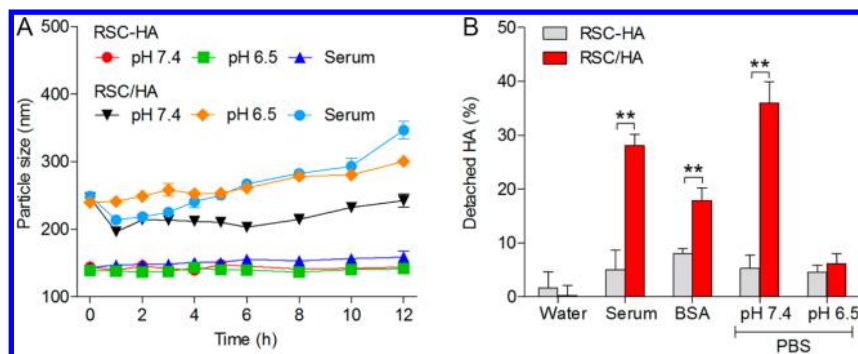


**Figure 3.** (A) Change in the particle size of RSC-HA and RSC/HA after incubation at pH 7.4 and 6.5 or in the presence of serum over time. RSC-HA was constructed by the collaborative assembly strategy, while RSC/HA was fabricated by the physical assembly approach. (B) Quantification of the HA detached from RSC-HA and RSC/HA under different conditions. \*\* $P < 0.01$ .

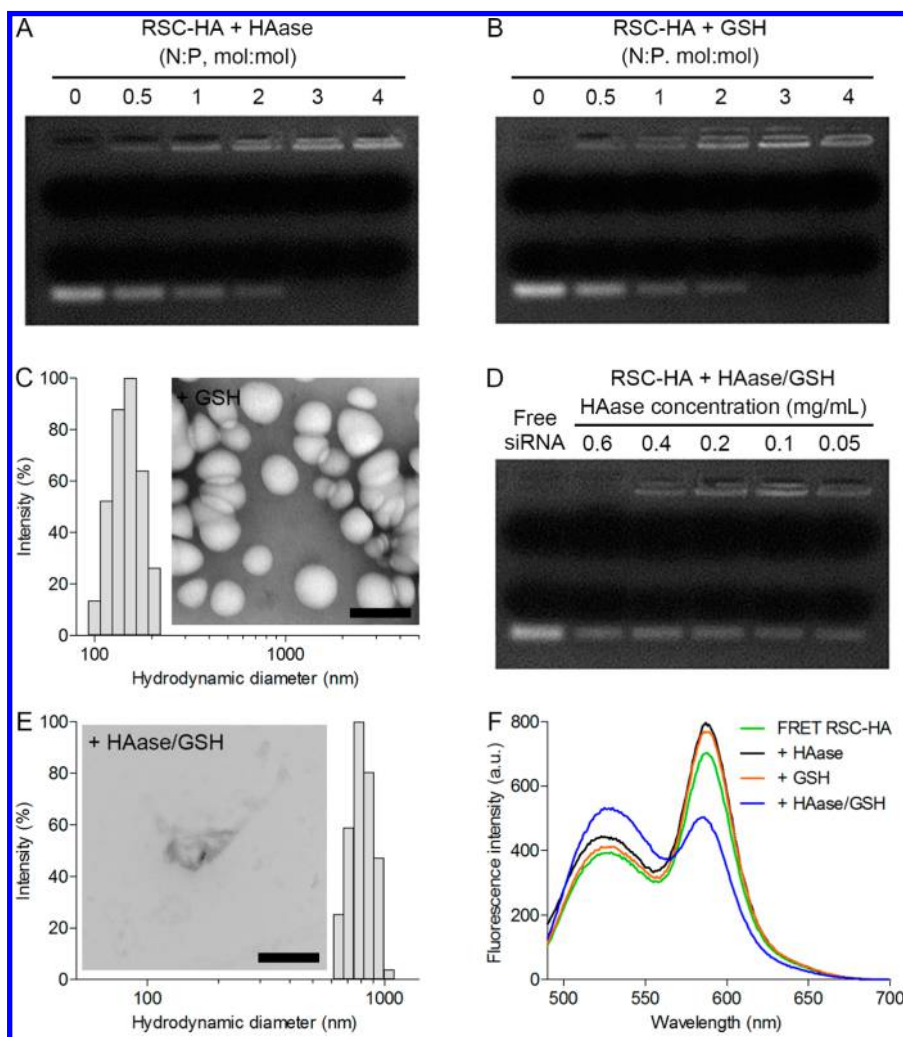


**Figure 4.** Agarose gel electrophoresis assay of RSC-HA at different N:P ratios after 2 h of incubation with (A) 0.5 mg/mL HAase for 2 h and (B) 10 mM GSH. (C) Size distribution histogram of RSC-HA after 2 h of incubation with 10 mM GSH using the DLS measurement. Inset: TEM image of the treated RSC-HA. Scale bar: 200 nm. (D) Agarose gel electrophoresis assay of RSC-HA after 2 h of incubation with different concentrations of HAase and another 2 h of incubation with 10 mM GSH. (E) Size distribution histogram of RSC-HA after 2 h of incubation with 0.5 mg/mL HAase and 10 mM GSH using the DLS measurement. Inset: TEM image of the treated RSC-HA. Scale bar: 500 nm. (F) Fluorescence spectra of the FRET RSC-HA at the excitation wavelength of 470 nm after 12 h of incubation with 0.5 mg/mL HAase or 10 mM GSH.

diameter of about 240 nm and a  $\zeta$  potential of  $-27$  mV at the N:P ratio of 4:1 (mol:mol) and the HA:Chol- $N_3$  ratio of 2:1 (mol:mol) (Figure S2A). RSC/HA could fully condense siRNA at the N:P ratio higher than 3:1 (Figure S2B). The variation in the particle size of RSC-HA and RSC/HA was monitored after

incubation under different conditions over time (Figure 3A). The particle size of RSC-HA maintained unchanged in the presence of serum or at pH 7.4 (physiological pH) and pH 6.5 (a typical tumor extracellular pH). By comparison, RSC/HA showed a large fluctuation in the particle size under the same

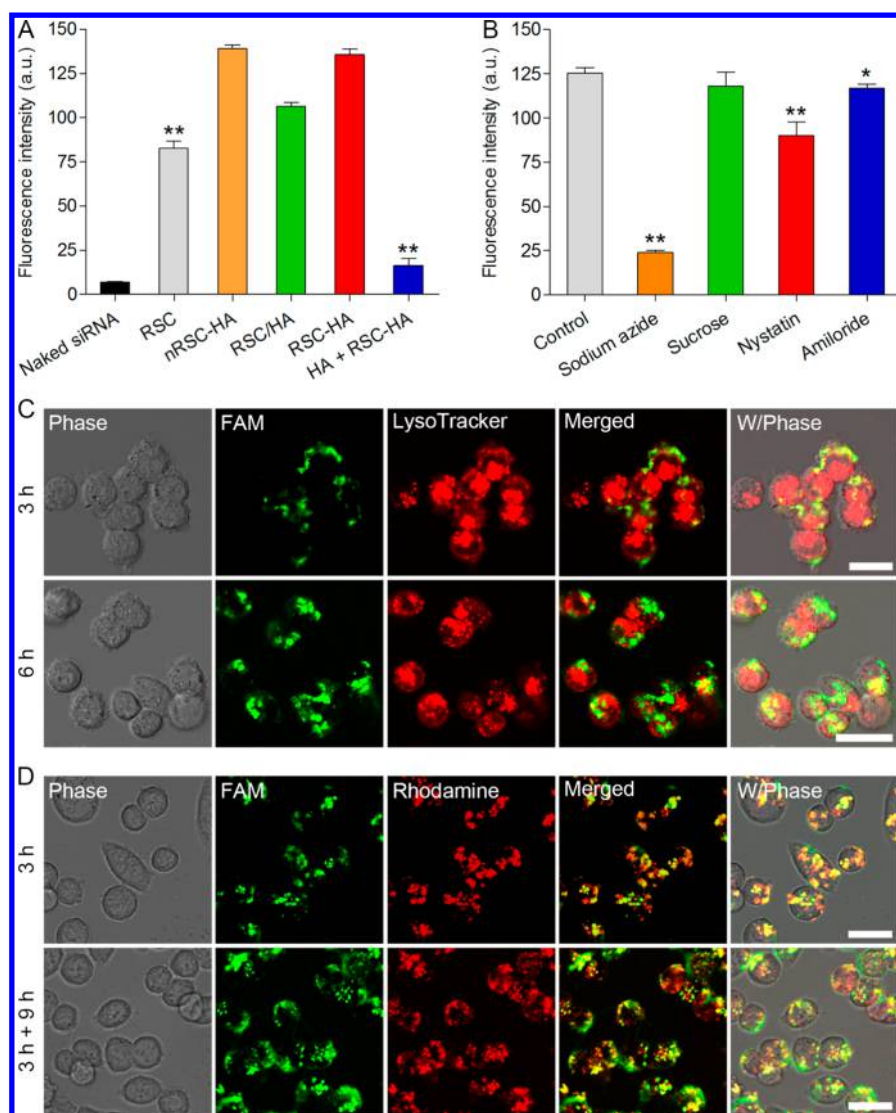


**Figure 5.** (A) Cellular uptake of FAM-siRNA delivered by different formulations determined using the flow cytometry.  $**P < 0.01$ , compared with RSC-HA. (B) Endocytosis pathway of RSC-HA loaded with FAM-siRNA determined using the flow cytometry.  $*P < 0.05$ ,  $**P < 0.01$ , compared with control. (C) Subcellular distribution of RSC-HA loaded with FAM-siRNA in A549 cells. The late endosomes and lysosomes were stained with LysoTracker Red. Scale bar:  $20 \mu\text{m}$ . (D) Intracellular disassembly of RhB-labeled RSC-HA loaded with FAM-siRNA in A549 cells. Scale bar:  $20 \mu\text{m}$ .

conditions, which was mainly attributed to the unstable HA outer layer. Furthermore, the change of the HA amount on the surface of RSC-HA and RSC/HA under a different set of circumstances was quantified using the cetyltrimethylammonium bromide (CTAB) turbidimetric method (Figure 3B).<sup>39</sup> The free HA shedding from the complex was separated using a size exclusion chromatography technique. Slight change in the HA amount on RSC-HA was determined after incubation, while RSC/HA presented a significantly decreased amount of HA. It was indicated that the chemically conjugated HA of RSC-HA was firmly anchored on the RSC surface for enhanced stability, compared with the physically bound HA of RSC/HA. Taken together, RSC-HA, possessing a superior stability than RSC/HA, can reduce the unspecific interactions with blood proteins and prolonged retention time in the circulation for elevated tumor targeting.

**Enzyme and Redox Combined-Triggered siRNA Release.** To explore the release of siRNA from RSC-HA under intracellular conditions, the EMSA analysis was applied after incubating RSC-HA in the presence and absence of HAase

and GSH, respectively. The HAase-mediated HA degradation was confirmed by the surface charge conversion of RSC-HA after treated with HAase ( $0.5 \text{ mg/mL}$ ) under acid condition as time extended (Figure S3A), which was due to the degraded small molecular HA pieces shedding from RSC. This result was in agreement with the quantitative assay (Figure S3B). However, since HAase degraded the HA shell, but the RSC core remained stable, and no free siRNA was visualized in the siRNA band after RSC-HA (N:P = 4:1, mol:mol) was incubated with HAase ( $0.5 \text{ mg/mL}$ ) alone (Figures 4A and S4A). On the other hand, only treatment with a high concentration of GSH ( $10 \text{ mM}$ , a typical concentration within the cells) also showed no release of siRNA from RSC-HA (Figure 4B), which implied that the HA shell held the inner RSC via the triazole linkages and hindered the siRNA release, although RSC was destabilized by the GSH-mediated LHSSG2C<sub>14</sub> cleavage. The TEM image confirmed the structural integrity of RSC-HA after the GSH treatment (Figure 4C). In sharp contrast, the released siRNA bands were clearly observed after incubation of RSC-HA with a variety of

concentrations of HAase in the presence of GSH (10 mM) (Figure 4D). Additionally, the treatment with HAase and GSH at the concentration of 1 or 10 mM resulted in the siRNA release from RSC-HA, while no released siRNA band was detected after incubation of RSC-HA with HAase in the presence of GSH (10  $\mu$ M) (a typical concentration outside the cells) (Figure S4B). The disruption of RSC-HA was further substantiated by the TEM imaging (Figure 4E). No spherical particles were visible after the combined treatment with HAase (0.5 mg/mL) and GSH (10 mM). It was suggested that the rapid disassociation of RSC-HA accompanied by the efficient release of siRNA was synergistically triggered by a combination of HAase and GSH inside the cells.

To further demonstrate the specificity of the siRNA release, RSC-HA was treated with both bovine serum albumin (BSA) and GSH, followed by the EMSA analysis. As expected, no free siRNA band was detected (Figure S5), which indicated that the negatively charged BSA was unable to competitively displace the HA shell conjugated on RSC and hardly induce the release of siRNA even with the help of GSH. In addition, a nonredox-sensitive complex (designated as nRSC-HA) was taken as a reference, which was prepared similarly as RSC-HA except that a control cationic lipid without disulfide linkage, LHG2C<sub>14</sub> was in place of LHSSG2C<sub>14</sub>. nRSC-HA had an average particle size of 139 nm and  $\zeta$  potential of  $-29$  mV at the N:P ratio of 4:1 (Figure S6A), which was capable of completely complexing siRNA (Figure S6B). After the HAase/GSH-combined treatment, nRSC-HA did not show any siRNA release (Figure S6C).

Next, we used a fluorescence resonance energy transfer (FRET) technique to estimate the integrity of RSC-HA exposed to the HAase/GSH environment. *N*-(7-Nitrobenz-2-oxa-1,3-diazol-4-yl)-1,2-dihexadecanoyl-*sn*-glycero-3-phosphoethanolamine (NBD-PE) and *N*-(lissamine rhodamine B sulfonyl)-1,2-dihexadecanoyl-*sn*-glycero-3-phosphoethanolamine (RhB-PE) were simultaneously pre-incorporated into the liposomal components to obtain the FRET RSC-HA. The change in the FRET signals allowed the detection of the integrity variation of RSC-HA. As shown in Figure 4F, the FRET RSC-HA showed an apparent emission of RhB at 585 nm after the NBD excitation at 470 nm, suggesting that the integrity of RSC-HA supported the energy transfer from the NBD donor to the RhB acceptor. Of note, treatment with either HAase or GSH had no remarkable impact on the stability of RSC-HA, while the dissociation of RSC-HA after the HAase/GSH-combined treatment was evidenced by the noticeably increased NBD signal together with the decreased RhB signal. Collectively, the highly stable RSC-HA impeded the siRNA leakage under physiological condition, while collapsed to efficiently release the encapsulated siRNA in response to combined stimuli, HAase and GSH, both of which were highly expressed inside the tumor cells.<sup>40,41</sup>

**Cellular Uptake, Subcellular Distribution, and Intracellular siRNA Release.** To verify the HA-mediated active targeting of RSC-HA (N:P = 4:1, mol:mol), the human lung adenocarcinoma epithelial (A549) cells, which overexpress the HA receptor, CD44 on the cell membrane,<sup>42</sup> were incubated with different formulations containing FAM-labeled siRNA (FAM-siRNA) for 6 h, followed by detecting the fluorescence intensity of FAM-siRNA within the cells using flow cytometry (Figure 5A). RSC noticeably facilitated the cellular uptake of siRNA upon the electrostatic attraction-based internalization compared with the naked siRNA. However, RSC-HA showed significantly enhanced uptake of siRNA than RSC without the

HA shell, which indicated that the CD44-mediated endocytosis played an important role in facilitating the intracellular accumulation of siRNA. Additionally, after the cells were pretreated with the excessive amount of free HA to block the CD44 receptor, the cellular uptake of RSC-HA drastically reduced, which further confirmed that RSC-HA could bind onto and enter into the cancer cells primarily via the CD44-mediated endocytosis.

The endocytotic pathway of RSC-HA was then determined by monitoring the change in the fluorescence intensity of siRNA after incubating the cells in the presence of different inhibitors for specific pathways (Figure 5B). Treatment with sodium azide, an energy inhibitor,<sup>43</sup> extremely reduced the cellular uptake of RSC-HA, indicating that RSC-HA permeated into the cells via a typical energy-dependent endocytotic pathway. The presence of both nystatin, the inhibitor of caveolae-mediated endocytotic pathway<sup>44</sup> and amiloride, the inhibitor of macropinocytosis,<sup>45</sup> exhibited a pronounced effect on inhibiting the cellular uptake of RSC-HA, suggesting that RSC-HA was localized in the caveosomes and macropinosomes after internalization and then transported into the endosomes.

The subcellular distribution of RSC-HA in A549 cells was examined using the confocal laser scanning microscope (CLSM) (Figure 5C). In the cells incubated with RSC-HA for 3 h, the signal of FAM-siRNA (green) encapsulated in RSC-HA was mainly colocalized with the signal of LysoTracker (red), a late endosome and lysosome marker, indicating that RSC-HA was effectively taken up by the cells and entrapped into the endosomes. After an additional 3 h of incubation, a great dissociation in the signals of FAM-siRNA and LysoTracker was observed, confirming the efficient endosomal escape of RSC-HA. This enhanced endosomal escape was associated with the proton sponge effect of the cationic histidine-containing lipid in RSC-HA,<sup>37,46</sup> which could gradually absorb protons, produce an increased osmotic pressure within the endosomes, and therefore cause the endosomal disruption, as confirmed by a buffering capacity assay (Figure S7).

To evaluate the intracellular release of siRNA, the fluorescence change was also detected using CLSM after the cells were incubated with the double-labeled RSC-HA containing FAM-siRNA and RhB-PE over time (Figure 5D). After 3 h of incubation, the signal of FAM-siRNA (green) was mostly overlaid with the signal of RhB-PE (red) that was used to label the nanocarrier, implying that siRNA was embedded in RSC-HA. Note that the FAM and RhB signals showed an obvious separation after incubation for additional 9 h, suggesting an efficient intracellular release and cytoplasmic distribution of siRNA due to the dissociation of RSC-HA in response to the intracellular HAase and GSH.

To further demonstrate the important role of HAase in the disassembly of RSC-HA in the cells, we applied a small-molecule inhibitor, thioguanine (TG)<sup>47</sup> to inhibit the effect of HAase on degrading HA and evaluated its inhibition effect on the HAase-mediated HA degradation. RSC-HA was incubated with HAase in the presence of different concentrations of TG over time, followed by determination of the HA degradation from RSC using the CTAB turbidimetric method (Figure S8). At the concentration of 4.5  $\mu$ M that has been proposed as the half maximal inhibitory concentration in the previous report,<sup>47</sup> TG showed an efficient capability of inhibiting HAase to degrade HA. When the concentration of TG was increased to higher than 9  $\mu$ M, the HA degradation by HAase was nearly

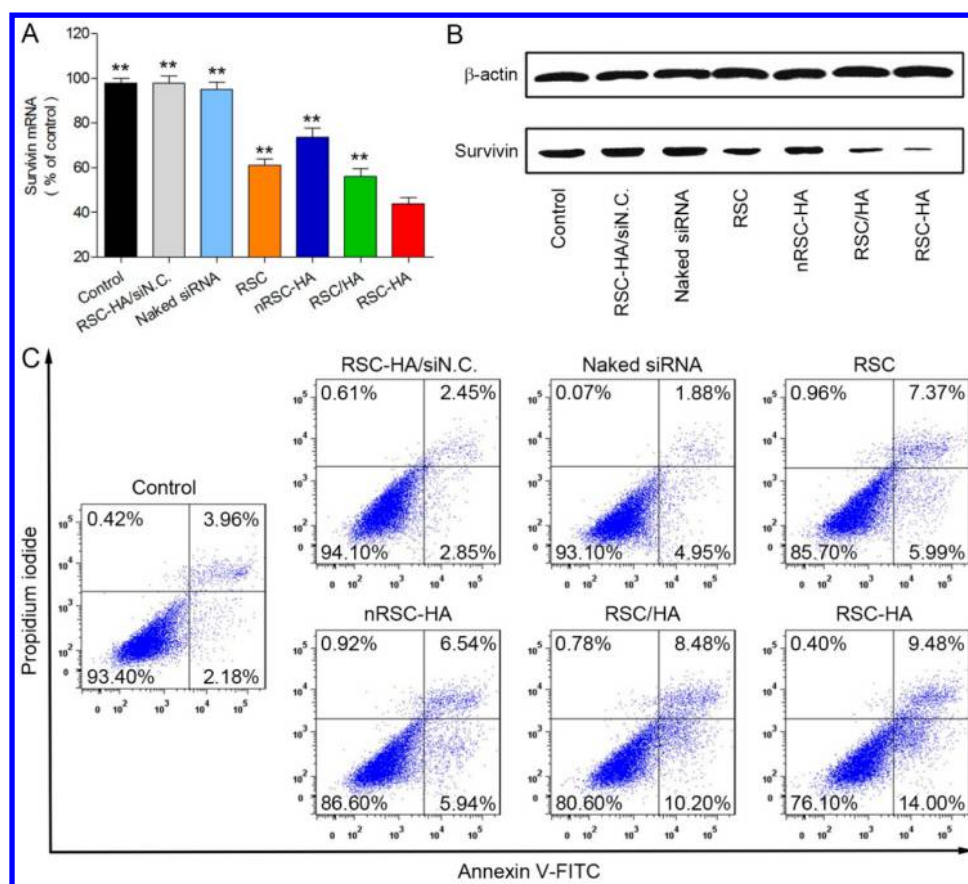


**Figure 6.** (A) Survivin mRNA expression determined by qRT-PCR.  $**P < 0.01$ , compared with RSC-HA. (B) Survivin protein expression determined by the Western blot analysis. (C) Cell apoptosis after transfection with different formulations determined by the Annexin V-FITC/PI assay. The viable, early apoptotic, and late apoptotic cell populations (%) are shown in the lower left, lower right, and upper right quadrants, respectively.

completely suppressed. Afterward, the FRET technique was applied to estimate the role of HAase in the destabilization of RSC-HA in cells. The cells were incubated with the FRET RSC-HA containing NBD-PE and RhB-PE in the absence and presence of TG ( $9 \mu\text{M}$ ) for different times, followed by monitoring the FRET change (Figure S9). After the cells were incubated with the FRET RSC-HA for 3 h, no significant change in the fluorescence spectra was found, while a noticeable increased NBD signal along with the decreased RhB signal were observed after incubation with the FRET RSC-HA for additional 9 h, which suggested the disassembly of RSC-HA inside the cells (Figure S9A). The FRET ratio  $[(I_{\text{RhB}})/(I_{\text{RhB}} + I_{\text{NBD}}) \times 100\%]$ <sup>48</sup> of RSC-HA in the cells reduced from 61.67% at 3 h to 50.06% at 3 h plus 9 h, where  $I_{\text{RhB}}$  and  $I_{\text{NBD}}$  are the fluorescence intensity of RhB at 585 nm and NBD at 530 nm, respectively (Figure S9B). In sharp contrast, the TG-treated cells presented no remarkable change in the fluorescence spectra between 3 and 3 h plus 9 h, suggesting that RSC-HA maintained the structural integrity inside the cells since TG inhibited the HAase-mediated HA degradation. The FRET ratio of RSC-HA showed no significant change as the incubation time increased after treatment with TG. Furthermore, the intracellular siRNA release accompanied by the disassembly of RSC-HA-containing FAM-siRNA and RhB-PE was monitored in the presence of TG using CLSM (Figure S9C). No apparent separation between the FAM and RhB signals was observed after the TG-treated cells were incubated

with RSC-HA for additional 9 h. As a result, HAase had a significant effect on the intracellular disintegration of RSC-HA.

#### Gene Silencing and Apoptosis Inducing Capability.

To evaluate the siRNA-mediated gene-silencing efficiency of RSC-HA, the level of mRNA (mRNA) transcription and the related protein expression were determined by the quantitative real-time polymerase chain reaction (qRT-PCR) and Western blot analysis, respectively (Figures 6 and S10). Survivin, an inhibitor of apoptosis protein, functions to negatively regulate cell apoptosis,<sup>49</sup> which is highly expressed in many cancer cells and associated with chemotherapy resistance.<sup>50</sup> A therapeutic siRNA targeting survivin mRNA (designed as cpusRNA2)<sup>51</sup> was encapsulated in RSC-HA. At the mRNA level, compared with other formulations, the RSC-HA loaded with cpusRNA2 showed the highest sequence-specific silencing efficiency on the survivin mRNA expression with 55.09% down-regulation in A549 cells (Figure 6A) and 65.02% in the murine Lewis lung cancer (LLC) cells that also overexpress CD44 receptor (Figure S10A), which validated that the enhanced cellular uptake and efficient intracellular delivery of siRNA by RSC-HA resulted in the elevated gene-silencing effectiveness. In line with this, at the protein expression level, cpusRNA2 delivered by RSC-HA remarkably decreased the expression of survivin protein in both of the lung cancer cells (Figure 6B and Figure S10B).

Next, we estimated the apoptosis-inducing effect of RSC-HA loaded with cpusRNA2 using the Annexin V-FITC/PI apoptosis detection. As expected, the cells after treatment

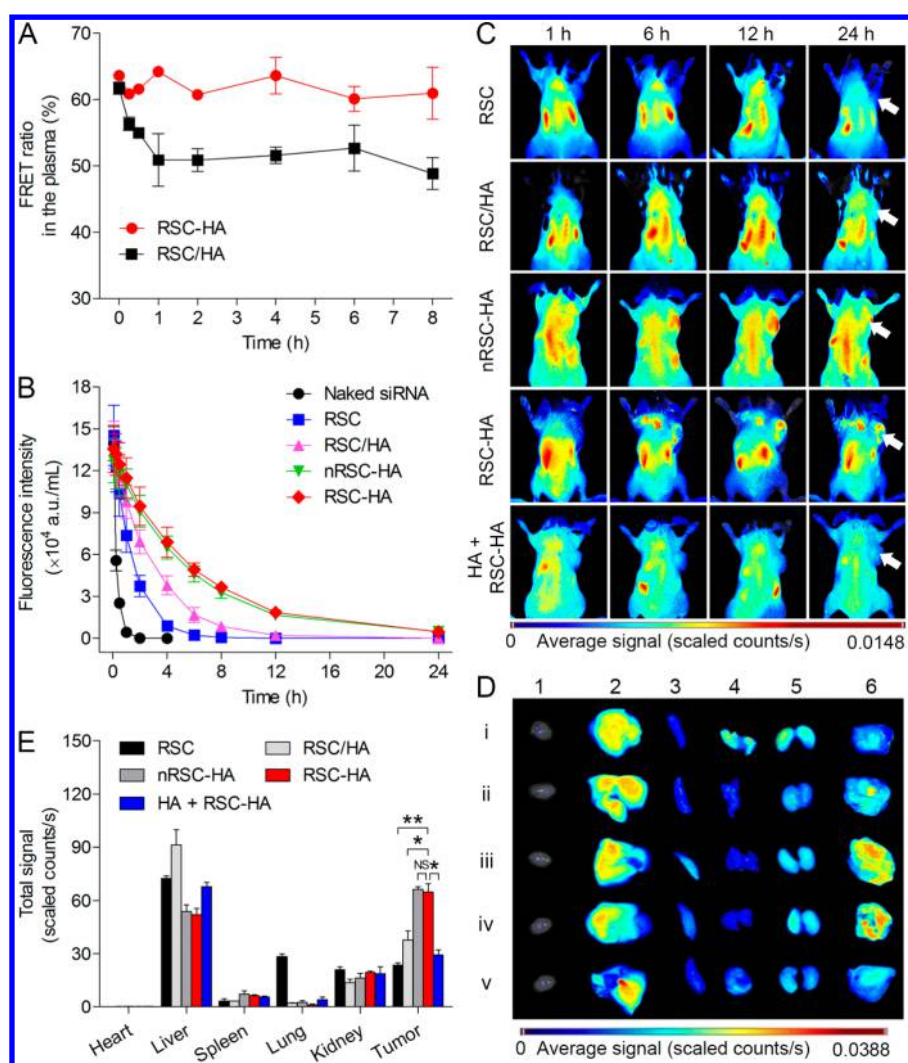


**Figure 7.** (A) Change in the FRET ratio of RSC-HA and RSC/HA in the plasma. The FRET ratio is indicated as  $I_{\text{RhB}}/(I_{\text{RhB}} + I_{\text{NBD}}) \times 100\%$ , where  $I_{\text{RhB}}$  and  $I_{\text{NBD}}$  are the fluorescence intensity of RhB at 575 nm and NBD at 530 nm, respectively. (B) Pharmacokinetics of FAM-siRNA after intravenous injection of different formulations into the rats. (C) *In vivo* biodistribution of Cy5-siRNA monitored using the *in vivo* imaging after intravenous injection of different formulations into the LLC tumor-bearing mice. The white arrows indicate the region of the tumor. (D) Accumulation of Cy5-siRNA in the tumor and different organs detected using the *ex vivo* imaging at 24 h post-injection of different formulations: (i) RSC; (ii) RSC/HA; (iii) nRSC-HA; (iv) RSC-HA; (v) HA+RSC-HA. (1) heart; (2) liver; (3) spleen; (4) lung; (5) kidney; (6) tumor. (E) Fluorescence intensity of Cy5-siRNA in the tumor and different organs quantified using the ROI analysis. \*\* $P < 0.01$ , \* $P < 0.05$ .

with RSC-HA loaded with cpusRNA2 showed the strongest apoptosis. The total apoptotic ratio, a sum of the early and late apoptotic ratios, was 23.48% in A549 cells (Figure 6C) and 60.7% in LLC cells (Figure S10C), much higher than that of other formulations. It is confirmed that RSC-HA with the high gene-silencing efficiency exhibited a superior apoptosis-inducing capacity.

**Pharmacokinetics, Biodistribution, Therapeutic Efficacy, and Safety Evaluation.** The FRET technique was first utilized to compare the stability of the conjugated HA on the collaboratively assembled RSC-HA with that of the adsorbed HA on the physically assembled RSC/HA during the systemic circulation (Figures 7A and S11). Both RSC-HA and RSC/HA were doubly labeled with NBD and RhB as a FRET pair, in which NBD-PE was anchored into the liposome to track the complex core and RhB was covalently conjugated to alk-HA (RhB-alk-HA) (Scheme S5) or HA (RhB-HA) (Scheme S6) to track the outer shell. When the HA shell was firmly coated on the complex core, the proximity between NBD and RhB was in

the FRET range, which supported the efficient energy transfer from NBD to RhB at the excitation of NBD at 470 nm (Figure S11A). The FRET ratio of RSC-HA and RSC/HA was calculated to be 63.62% and 61.70%, respectively. After intravenous injection of the FRET nanocarriers into the rats for different time, the change in the fluorescence signals in the plasma was monitored. The FRET signal maintained up to 8 h in RSC-HA (Figure S11B), while the attenuation in the FRET effect as the increased NBD signal with the decreased RhB signal was apparently observed in RSC/HA (Figure S11C). The FRET ratio of RSC/HA rapidly reduced to 50.91% within 1 h post-injection, indicating that the adsorbed HA shell was unstable and underwent shedding from RSC/HA in the circulation (Figure 7A). In contrast, the FRET ratio of RSC-HA retained stable within the studied time period, suggesting that the chemical conjugation significantly enhanced the *in vivo* stability of the HA shell.

The pharmacokinetics was investigated after intravenous injection of different formulations containing FAM-siRNA

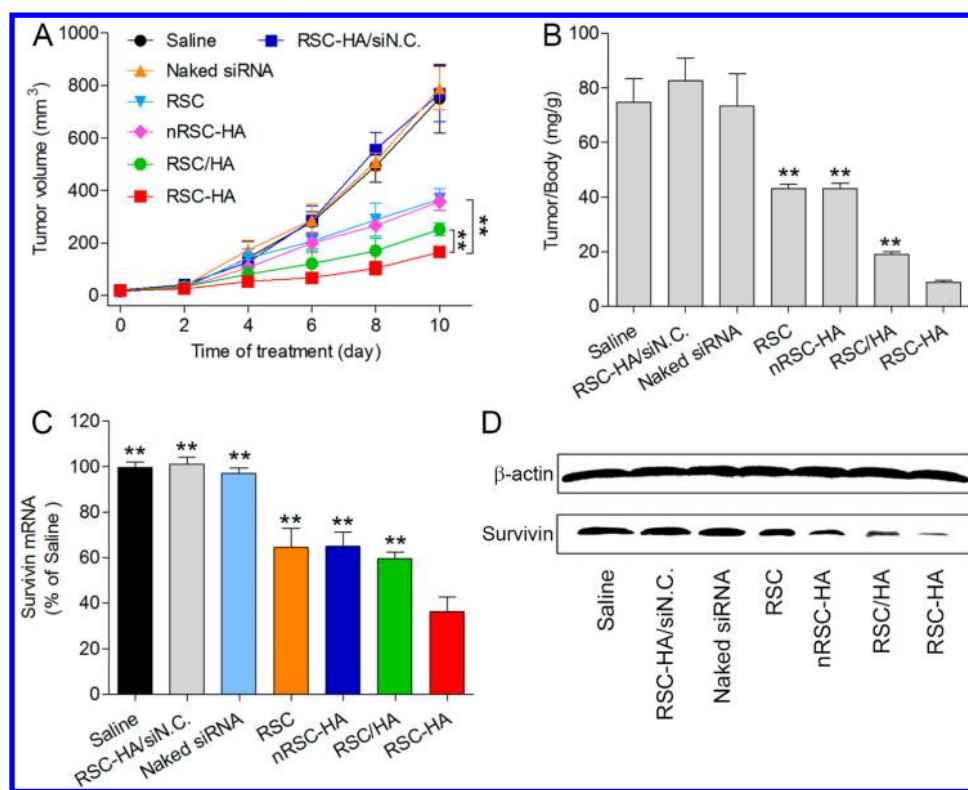


**Figure 8.** (A) Change in the tumor size of the LLC tumor-bearing mice receiving intravenous injection of different formulations at a dose of 1.2 mg/kg.  $**P < 0.01$ . (B) Weight ratio of the tumor to the body of the mice after treatment.  $**P < 0.01$ , compared with RSC-HA. (C) Survivin mRNA expression in the tumor harvested from the mice after treatment determined by qRT-PCR.  $**P < 0.01$ , compared with RSC-HA. (D) Survivin protein expression in the tumor harvested from the mice after treatment determined by the Western blot analysis.

(Figure 7B and Table S1). Compared with the encapsulated siRNA in the complex, the naked siRNA showed an extremely rapid degradation and clearance in the body, which had a half-time ( $t_{1/2}$ ) of only 0.26 h. The HA outer shell of RSC/HA, nRSC-HA, and RSC-HA increased the *in vivo* stability of RSC and rendered the long circulating behavior. More importantly, RSC-HA displayed a conspicuously enhanced blood persistence than RSC/HA, which had a higher area under the plasma concentration versus the time curves (AUC), longer  $t_{1/2}$  and mean residence time (MRT), and a lower clearance (Cl). Nevertheless, the pharmacokinetic parameters of RSC-HA were similar to that of nRSC-HA. It is speculated that the chemically conjugated HA shell holds the complex core more firmly than the physically adsorbed one, thereby increasing the bioavailability of siRNA in the blood for potential reinforcement of the tumor targeting and antitumor effect.

To assess the tumor targeting property of RSC-HA, we applied an *in vivo* fluorescence imaging technique to detect the biodistribution of RSC-HA loaded with Cy5-conjugated siRNA (Cy5-siRNA) after intravenous injection into the LLC tumor-bearing mice (Figure 7C). RSC-HA showed greater tumor targetability than both RSC and RSC/HA, while no significant difference was found in the effect between RSC-HA and nRSC-HA. The Cy5 signal of RSC-HA was clearly observed at the tumor site at 6 h post-injection and maintained for up to 24 h. It is suggested that the enhanced HA shell via the chemical conjugation realized the efficient and tumor-targeted intravenous siRNA delivery. To further demonstrate the HA-mediated tumor targetability of RSC-HA, a high dose of the free HA was intravenously pre-administrated into the mice followed by the injection of RSC-HA. The Cy5 signal was

monitored to be much weaker in the tumor region after pre-injection of HA as expected; this is because the free HA competitively blocked the binding between RSC-HA and the CD44 receptors, which resulted in the decreased tumor accumulation of RSC-HA. At 24 post-injection, the tumor and different organs were collected for *ex vivo* imaging (Figure 7D). The Cy5 signal of RSC-HA at the tumor site was noticeably higher than that of RSC, RSC/HA, and the HA pre-injected RSC-HA but comparable to that of nRSC-HA. The quantitative region-of-interest (ROI) analysis further substantiated the superior tumor targeting ability of RSC-HA (Figure 7E), which showed the Cy5 intensity with 2.7-, 1.7-, and 2.2-fold of RSC, RSC/HA and the HA pre-injected RSC-HA at the tumor site, respectively. Additionally, the Cy5 intensity of RSC-HA at the tumor site was 392.4-, 1.2-, 10.2-, 58.9-, and 3.3-fold of that at heart, liver, spleen, lung, and kidney, respectively. There was no significant difference in the Cy5 intensity between RSC-HA and nRSC-HA. The liver accumulation of RSC-HA containing FAM-siRNA and RhB-alk-HA was monitored after injection for different time (Figure S12). The liver sinusoidal endothelial cells (LSECs) specifically expressing CD146 receptors<sup>52</sup> in the liver section were stained with the APC-conjugated CD146 antibody. At 1 h post-injection, RSC-HA showed a clear liver accumulation, a large part of which was rapidly taken up by the LSECs, as substantiated by the colocalization of the FAM-siRNA (green), RhB-labeled HA (red), and CD146 (purple) expressing LSECs. As time extended, both of FAM and RhB signals gradually attenuated and almost disappeared at 24 h post-injection, indicating the metabolism and excretion of RSC-HA by the liver. Furthermore, the intratumoral distribution of RSC-HA

containing RhB-PE and Cy5-siRNA was also investigated at 24 h post-injection (Figure S13). The CD44 receptors in the tumor section were stained with the FITC-conjugated CD44 antibody. Cy5-siRNA (red) and RhB-labeled carrier (purple) of RSC-HA distributed throughout the tumor and closely associated with CD44 (green) overexpressing cells, which implied that RSC-HA could effectively deliver the encapsulated siRNA into the tumor region.

The therapeutic potential of RSC-HA loaded with cpusiRNA2 was evaluated on the LLC tumor-bearing mice (Figure 8). Nanoparticle-based formulations loaded with cpusiRNA2 exhibited stronger effects on inhibiting the tumor growth, compared with the control groups, such as saline, the naked cpusiRNA2 and RSC-HA/siN.C. (Figures 8A and S14). Note that a significant difference in the tumor growth inhibition was determined between RSC-HA and RSC/HA, suggesting that the *in vivo* stability of the HA shell on the complex played an essential part in the tumor-targeted delivery of siRNA and the improved therapeutic efficacy. Moreover, RSC-HA showed higher tumor growth-inhibiting effect than nRSC-HA, indicating that the efficient intracellular release of siRNA contributed to the enhanced antitumor activity. The body weight of the mice did not show obvious change during the period of treatment with RSC-HA (Figure S15). At the end of treatment, the tumors were harvested and weighed. The mice treated with RSC-HA presented much lower mass ratio of the tumor to the body, compared with other formulations (Figure 8B). Treatment with the RSC-HA loaded with cpusiRNA2 presented the highest sequence-specific silencing efficiency on the survivin mRNA expression with 63.70% down-regulation (Figure 8C) and remarkably decreased the expression of survivin protein in the tumor (Figure 8D). In addition, the hematoxylin and eosin (HE) stained tumor section for histological analysis showed a large area of cancer cells remission after the mice received the treatment of RSC-HA (Figure S16A). The apoptosis detection using the terminal deoxynucleotidyl transferase dUTP nick end labeling (TUNEL) assay confirmed that treatment with the RSC-HA carrying survivin-targeted siRNA produced greater apoptosis for efficiently suppressing the tumor growth (Figure S16B).

For the safety evaluation, the quantities of alkaline phosphatase (AKP), alanine transaminase (ALT), aspartate transaminase (AST) for liver toxicity, and blood urea nitrogen (BUN) for kidney toxicity in the plasma were determined after RSC-HA treatment in comparison with that after treatment with saline, respectively (Figure S17). No significant difference in the amount of AKP, ALT, AST, and BUN between RSC-HA and saline was observed. Meanwhile, the main normal organs were harvested and weighed, such as heart, liver, spleen, lung, kidney, and thymus. The mice treated with RSC-HA did not show any noticeable variation in the mass ratio of the organ to the body (Figure S18A). Furthermore, the histological analysis on the liver, spleen, and kidney using the HE staining evidenced that treatment with RSC-HA displayed no pathological change compared with treatment with saline (Figure S18B). In addition, no gene silencing caused by RSC-HA was determined in the liver, spleen, and kidney compared with that in the tumor (Figure S19). These results suggested that RSC-HA was a safe and potential nanocarrier for the efficient siRNA delivery within the studied time period.

## CONCLUSIONS

In summary, we have developed a novel “collaborative assembly” strategy for a tumor-targeted siRNA delivery system based on a combination of physical and chemical assembly. RSC-HA was successfully fabricated by directly conjugating the polyanionic HA polymer on the surface of the cationic lipid-based complex with siRNA via click chemistry, which showed greater *in vivo* stability in the blood for efficient tumor targeting, compared with RSC/HA in which HA was physically adsorbed on the complex. The protection of RSC-HA on siRNA turned off inside the cells and the release of siRNA activated by the intracellular signals for enhanced therapeutic efficacy. This assembly approach resolved the conflict among toxicities, siRNA binding efficiency, and stability related to the cationic property of the complex. We anticipate this strategy will provide a promising platform for the easy-to-fabrication of effective siRNA delivery systems and potentially promote the clinical application of siRNA therapy.

## ASSOCIATED CONTENT

### Supporting Information

Experimental procedures and *in vitro* and *in vivo* characterization of the nanocarrier. This material is available free of charge via the Internet at <http://pubs.acs.org>.

## AUTHOR INFORMATION

### Corresponding Authors

\*zhangcan@cpu.edu.cn

\*rmo@cpu.edu.cn

### Notes

The authors declare no competing financial interest.

## ACKNOWLEDGMENTS

This work was supported by the National Natural Science Foundation of China (81473153, 81273468), National Basic Research Program of China (2015CB755500), State Key Laboratory of Natural Medicines at China Pharmaceutical University (SKLNMZZCX201401), 111 Project from the Ministry of Education of China and the State Administration of Foreign Expert Affairs of China (no. 111-2-07), and Natural Science Foundation of Jiangsu Province of China (BK20140672).

## REFERENCES

- (1) Fire, A.; Xu, S.; Montgomery, M. K.; Kostas, S. A.; Driver, S. E.; Mello, C. C. *Nature* **1998**, *391*, 806.
- (2) Whitehead, K. A.; Langer, R.; Anderson, D. G. *Nat. Rev. Drug Discovery* **2009**, *8*, 516.
- (3) Salcher, E. E.; Wagner, E. *Top. Curr. Chem.* **2010**, *296*, 227.
- (4) Whitehead, K. A.; Dorkin, J. R.; Vegas, A. J.; Chang, P. H.; Veisheh, O.; Matthews, J.; Fenton, O. S.; Zhang, Y. L.; Olejnik, K. T.; Yesilyurt, V.; Chen, D. L.; Barros, S.; Klebanov, B.; Novobrantseva, T.; Langer, R.; Anderson, D. G. *Nat. Commun.* **2014**, *5*, 4277.
- (5) Nomoto, T.; Fukushima, S.; Kumagai, M.; Machitani, K.; Arnida; Matsumoto, Y.; Oba, M.; Miyata, K.; Osada, K.; Nishiyama, N.; Kataoka, K. *Nat. Commun.* **2014**, *5*, 3545.
- (6) Guo, X.; Huang, L. *Acc. Chem. Res.* **2012**, *45*, 971.
- (7) Cui, L.; Cohen, J. L.; Chu, C. K.; Wich, P. R.; Kierstead, P. H.; Frechet, J. M. J. *Am. Chem. Soc.* **2012**, *134*, 15840.
- (8) Pecot, C. V.; Calin, G. A.; Coleman, R. L.; Lopez-Berestein, G.; Sood, A. K. *Nat. Rev. Cancer* **2011**, *11*, 59.
- (9) Thompson, J. D. *Drug Discovery Today: Ther. Strategies* **2013**, *10*, e133.

- (10) Thomas, C. E.; Ehrhardt, A.; Kay, M. A. *Nat. Rev. Genet.* **2003**, *4*, 346.
- (11) Niidome, T.; Huang, L. *Gene Ther.* **2002**, *9*, 1647.
- (12) Descamps, D.; Benihoud, K. *Curr. Gene Ther.* **2009**, *9*, 115.
- (13) Duerner, L. J.; Schwantes, A.; Schneider, I. C.; Cichutek, K.; Buchholz, C. J. *Gene Ther.* **2008**, *15*, 1500.
- (14) Schroeder, A.; Levins, C. G.; Cortez, C.; Langer, R.; Anderson, D. G. *J. Int. Med.* **2010**, *267*, 9.
- (15) Howard, K. A. *Adv. Drug Delivery Rev.* **2009**, *61*, 710.
- (16) Yang, X.; Du, J.; Dou, S.; Mao, C.; Long, H.; Wang, J. *ACS Nano* **2011**, *6*, 771.
- (17) Ornelas-Megiatto, C.; Wich, P. R.; Frechet, J. M. *J. Am. Chem. Soc.* **2012**, *134*, 1902.
- (18) Yu, T.; Liu, X.; Bolcato-Bellemin, A. L.; Wang, Y.; Liu, C.; Erbacher, P.; Qu, F.; Rocchi, P.; Behr, J. P.; Peng, L. *Angew. Chem., Int. Ed.* **2012**, *51*, 8478.
- (19) Zhang, S.; Zhao, B.; Jiang, H.; Wang, B.; Ma, B. *J. Controlled Release* **2007**, *123*, 1.
- (20) Ozpolat, B.; Sood, A. K.; Lopez-Berestein, G. *Adv. Drug Delivery Rev.* **2014**, *66*, 110.
- (21) Ballarín-González, B.; Howard, K. A. *Adv. Drug Delivery Rev.* **2012**, *64*, 1717.
- (22) Wang, Y.; Xu, Z.; Zhang, R.; Li, W.; Yang, L.; Hu, Q. *Colloids Surf., B* **2011**, *84*, 259.
- (23) Al-Qadi, S.; Alatorre-Meda, M.; Zaghoul, E. M.; Taboada, P.; Remunán-López, C. *Colloids Surf., B* **2013**, *103*, 615.
- (24) Ballarín-González, B.; Howard, K. A. *Adv. Drug Delivery Rev.* **2012**, *64*, 1717.
- (25) Hashimoto, Y.; Abu Lila, A. S.; Shimizu, T.; Ishida, T.; Kiwada, H. *J. Controlled Release* **2014**, *184*, 1.
- (26) Huang, Y.; Lin, D.; Jiang, Q.; Zhang, W.; Guo, S.; Xiao, P.; Zheng, S.; Wang, X.; Chen, H.; Zhang, H.-Y.; Deng, L.; Xing, J.; Du, Q.; Dong, A.; Liang, Z. *Biomaterials* **2012**, *33*, 4653.
- (27) Ran, R.; Liu, Y.; Gao, H.; Kuang, Q.; Zhang, Q.; Tang, J.; Huang, K.; Chen, X.; Zhang, Z.; He, Q. *Int. J. Pharm.* **2014**, *477*, 590.
- (28) Buyens, K.; De Smedt, S. C.; Braeckmans, K.; Demeester, J.; Peeters, L.; van Grunsvan, L. A.; de Mollerat du Jeu, X.; Sawant, R.; Torchilin, V.; Farkasova, K.; Ogris, M.; Sanders, N. N. *J. Controlled Release* **2012**, *158*, 362.
- (29) Hatakeyama, H.; Akita, H.; Ito, E.; Hayashi, Y.; Oishi, M.; Nagasaki, Y.; Danev, R.; Nagayama, K.; Kaji, N.; Kikuchi, H.; Baba, Y.; Harashima, H. *Biomaterials* **2011**, *32*, 4306.
- (30) Abu Lila, A. S.; Kiwada, H.; Ishida, T. *J. Controlled Release* **2013**, *172*, 38.
- (31) De Koker, S.; Hoogenboom, R.; De Geest, B. G. *Chem. Soc. Rev.* **2012**, *41*, 2867.
- (32) de Villiers, M. M.; Otto, D. P.; Strydom, S. J.; Lvov, Y. M. *Adv. Drug Delivery Rev.* **2011**, *63*, 701.
- (33) Kluger, R. *J. Am. Chem. Soc.* **2010**, *132*, 6611.
- (34) Jiang, T.; Sun, W.; Zhu, Q.; Burns, N. A.; Khan, S. A.; Mo, R.; Gu, Z. *Adv. Mater.* **2015**, *27*, 1021.
- (35) Mo, R.; Jiang, T.; DiSanto, R.; Tai, W.; Gu, Z. *Nat. Commun.* **2014**, *5*, 3364.
- (36) Jiang, T.; Mo, R.; Bellotti, A.; Zhou, J.; Gu, Z. *Adv. Funct. Mater.* **2014**, *24*, 2295.
- (37) Mo, R.; Sun, Q.; Xue, J.; Li, N.; Li, W.; Zhang, C.; Ping, Q. *Adv. Mater.* **2012**, *24*, 3705.
- (38) Wu, W.; Yao, W.; Wang, X.; Xie, C.; Zhang, J.; Jiang, X. *Biomaterials* **2015**, *39*, 260.
- (39) Qhattal, H. S.; Liu, X. *Mol. Pharmaceutics* **2011**, *8*, 1233.
- (40) Stern, R.; Jedrzejewski, M. *J. Chem. Rev.* **2006**, *106*, 818.
- (41) Balendiran, G. K.; Dabur, R.; Fraser, D. *Cell Biochem. Funct.* **2004**, *22*, 343.
- (42) Kim, E.; Yang, J.; Park, J.; Kim, S.; Kim, N. H.; Yook, J. I.; Suh, J. S.; Haam, S.; Huh, Y. M. *ACS Nano* **2012**, *6*, 8525.
- (43) Fazlollahi, F.; Angelow, S.; Yacobi, N. R.; Marchelletta, R.; Yu, A. S.; Hamm-Alvarez, S. F.; Borok, Z.; Kim, K. J.; Crandall, E. D. *Nanomedicine: NBM* **2011**, *7*, 588.
- (44) Dudleamjil, E.; Lin, C. Y.; Dredge, D.; Murray, B. K.; Robison, R. A.; Johnson, F. B. *J. Gen. Virol.* **2010**, *91*, 3032.
- (45) Koivusalo, M.; Welch, C.; Hayashi, H.; Scott, C. C.; Kim, M.; Alexander, T.; Touret, N.; Hahn, K. M.; Grinstein, S. *J. Cell Biol.* **2010**, *189*, 547.
- (46) Shigeta, K.; Kawakami, S.; Higuchi, Y.; Okuda, T.; Yagi, H.; Yamashita, F.; Hashida, M. *J. Controlled Release* **2007**, *118*, 262.
- (47) Shen, M.; Chao, C.; Wu, Y.; Wu, Y.; Huang, C.; Li, Y. *Sens. Actuators, B* **2013**, *181*, 605.
- (48) Li, Y.; Xiao, W.; Xiao, K.; Berti, L.; Luo, J.; Tseng, H. P.; Fung, G.; Lam, K. S. *Angew. Chem., Int. Ed.* **2012**, *51*, 2864.
- (49) Altieri, D. C. *Oncogene* **2003**, *22*, 8581.
- (50) Kanwar, R. K.; Cheung, C. H.; Chang, J. Y.; Kanwar, J. R. *Curr. Med. Chem.* **2010**, *17*, 1509.
- (51) Lu, Y.; Wang, K.; He, R.; Xi, T. *Cancer Biother. Radiopharm.* **2008**, *23*, 727.
- (52) Mandili, G.; Alchera, E.; Merlin, S.; Imarisio, C.; Chandrashekar, B. R.; Riganti, C.; Bianchi, A.; Novelli, F.; Follenzi, A.; Carini, R. *J. Hepatol.* **2015**, *62*, 573.